J. Non-Newtonian Fluid Mech. 165 (2010) 362–375

Contents lists available at ScienceDirect

Journal of Non-Newtonian Fluid Mechanics

journal homepage: www.elsevier.com/locate/jnnfm

A numerical study of the flow of Bingham-like fluids in two-dimensional vane and cylinder rheometers using a smoothed particle hydrodynamics (SPH) based method

Huaning Zhu[a,b,*], Nicos S. Martys[a], Chiara Ferraris[a], Daniel De Kee[b]

[a] Materials and Construction Research Division, National Institute of Standards and Technology, 100 bureau Dr., Mail stop 8615, Gaithersburg, MD 20899, USA
[b] Department of Chemical and Biomolecular Engineering, Tulane University, New Orleans, LA 70118, USA

ARTICLE INFO

Article history:
Received 1 February 2008
Received in revised form 11 January 2010
Accepted 12 January 2010

Keywords:
Vane rheometer
Smoothed particle hydrodynamics (SPH)
Bingham fluid
Non-Newtonian fluid
Papanastasiou model

ABSTRACT

In this paper, a Lagrangian formulation of the Navier–Stokes equations, based on the smoothed particle hydrodynamics (SPH) approach, was applied to determine how well rheological parameters such as plastic viscosity can be determined from vane rheometer measurements. First, to validate this approach, a Bingham/Papanastasiou constitutive model was implemented into the SPH model and tests comparing simulation results to well established theoretical predictions were conducted. Numerical simulations for the flow of fluids in vane and coaxial cylinder rheometers were then performed. A comparison to experimental data was also made to verify the application of the SPH method in realistic flow geometries. Finally, results are presented from a parametric study of the flow of Bingham fluids with different yield stresses under various applied angular velocities of the outer cylindrical wall in the vane and coaxial cylinder rheometers. The stress, strain rate and velocity profiles, especially in the vicinity of the vane blades, were computed. By comparing the calculated stress and flow fields between the two rheometers, the validity of the assumption that the vane could be approximated as a cylinder for measuring the rheological properties of Bingham fluids at different shear rates was tested.

1. Introduction

Vane geometries are commonly used to determine the rheological properties of many non-Newtonian fluids that can be characterized as having a shear rate dependent viscosity and so-called yield stress. However, due to the complex flow geometry of the vane, relating the measured quantities (torque and angular velocity) to the rheological properties (yield stress and viscosity) represents a significant challenge, partly because of various artifacts of measurement such as slip at fluid/wall boundaries and, perhaps more importantly, a lack of knowledge of the actual local flow rates. Indeed, the vane geometry has been primarily used in yield stress measurements for fluids that possess a yield stress and show slip at solid walls [1,2]. There are a number of advantages of the vane method over the use of conventional rheometers for structured materials, for example, less disturbance to the sample being measured; less susceptibility to artifacts arising from large particle sizes and alleviation of wall-depletion effect [3].

Several researchers [4–6] have found that the no-secondary-flow assumption at relatively low shear rates ($\sim 1\ s^{-1}$) for the vane is valid. However, their conclusion cannot be generalized to applications of rheological property measurements involving higher shear rates. Barnes and Carnali [3] addressed the suitability of the use of a vane geometry as a rheometer for shear thinning fluids and found that for a shear thinning fluid with a shear thinning (power) index greater than 0.5, the vane represents a good means of measuring the rheological properties of such fluids under steady flow conditions.

The interpretation of the experimental results is not always easy due to the lack of an analytical solution to extract shear rates and shear stresses in fundamental units. Therefore, a numerical simulation, predicting the bulk and interfacial properties of complex fluids, has been used to complement and guide experimentation. Numerical simulations of non-Newtonian flows in complex geometries have often been based on a macroscopic approach where one numerically solves the conservation laws together with a suitable rheological constitutive equation. In this area, many numerical approaches have been proposed, generally based on finite difference, finite element (FEM), finite volume (FVM) or boundary element methods (BEM). All of these numerical methods are, in essence, Eulerian schemes. As an alternative to classical Eulerian methods, Lagrangian based approaches avoid the complicated eval-

* Corresponding author at: Department of Fiber Science and Apparel design, Cornell University, Ithaca, NY 14853 USA.
E-mail address: hz222@cornell.edu (H. Zhu).

0377-0257/$ – see front matter © 2010 Elsevier B.V. All rights reserved.
doi:10.1016/j.jnnfm.2010.01.012

uation of advective terms and allow for tracing the motion of solid–fluid interfaces and simulating free surface flows without additional difficulty. Since our long-term goal is to simulate multiphase complex fluids such as suspensions with a non-Newtonian matrix, we decide to adopt a Lagrangian approach in the numerical computation. The SPH method [7,8], which is based on a fully Lagrangian formalism, has been successfully applied to different physical situations including multiphase flow [9–12], flow of geomaterials [13,14], fluid-structure interactions [15] and flow of visco-elastic fluids [16–18].

In the present study, a SPH numerical simulation for the flow of Bingham fluids in a vane rheometer was performed under relatively high shear rates in order to validate the suitability for measuring general rheological properties. The SPH algorithm was first verified in plane Poiseuille flow and in rotational Couette flow problems by comparing the simulation results to theoretical predictions. Then, numerical simulations were performed for the flow of a Newtonian fluid in vane and coaxial cylinder rheometers and the ratio of the shear stresses on the outer walls of the coaxial cylinders and the vane under different flow conditions was computed. Qualitative good agreement was achieved between the simulation results and the experimental data. In addition, a parametric study was conducted for Bingham fluids with different yield stresses under various applied angular velocities of the outer cylindrical wall. The effects of the Bingham number and the magnitude of the angular velocities on the vane-flow properties were investigated and the validity of the assumption that the vane could be approximated as a cylinder for measuring the rheological properties of Bingham fluids at different shear rates was assessed. Results presented in this paper will be limited to the case of two-dimensional flows. However, as outlined in the following sections, a two-dimensional numerical analysis is sufficient to indicate inherent problems with the suitability of using the vane rheometer to measure the plastic viscosity.

2. Governing equations

The tensorial continuum and momentum equations have the form

$$\frac{d\rho}{dt} = -\rho\nabla\cdot\boldsymbol{v}, \tag{1}$$

$$\rho\frac{d\boldsymbol{v}}{dt} = \nabla\cdot\boldsymbol{P} + \boldsymbol{b}, \tag{2}$$

where ρ is the density, $\boldsymbol{v}$ is the velocity, $\boldsymbol{b}$ is the body force, and the total stress tensor

$$\boldsymbol{P} = -p\boldsymbol{I} + \tau, \tag{3}$$

where p is the hydrostatic pressure at equilibrium and $\boldsymbol{\tau}$ is the extra stress tensor. For an idealized Bingham fluid, the constitutive equation can be written as:

$$\tau = \left(\eta + \frac{\tau_0}{\dot\gamma}\right)\dot\gamma \quad \text{for } \tau > \tau_0,$$

$$\dot\gamma = 0 \quad \text{for } \tau < \tau_0, \tag{4}$$

where $\dot\gamma$ is the strain rate tensor, η is the plastic viscosity, τ_0 is the yield stress, the effective strain rate and stress are defined as $\dot\gamma = \sqrt{(1/2)\dot{\boldsymbol{\gamma}}':\dot{\boldsymbol{\gamma}}'} = \sqrt{(1/2)\dot\gamma'_{ij}\dot\gamma'_{ij}}$ and $\tau = \sqrt{(1/2)\tau':\tau'} = \sqrt{(1/2)\tau'_{ij}\tau'_{ij}}$. Deviatoric strain rate tensor $\dot{\boldsymbol{\gamma}}'$ and stress tensor $\boldsymbol{\tau}'$ are defined as $\dot\gamma' = \dot\gamma - (1/2)(\dot\gamma_{ii})$ and $\boldsymbol{\tau}' = \boldsymbol{\tau} - (1/2)(\tau_{ii})$, respectively. It is difficult to apply the Bingham model directly in numerical simulations, especially in complex geometries. The difficulty is mainly due to the discontinuity in the constitutive relations; specifically, as the yield point is approached, the presence of the shear rate in the denominator of the Bingham model (Eq. (4)) makes the apparent viscosity diverge. Furthermore, while calculating the velocity field, the shape and location of the yield surface are unknown. Papanastasiou [19] proposed a regularized Bingham model to overcome the numerical difficulties. The regularized model is continuous and applies to both the yielded and unyielded regions. Alexandrou et al. [20], Burgos et al. [21] and Zhu and De Kee [22] discussed the validity of the regularized Bingham model. The regularized Bingham model can be written as:

$$\tau = \left(\eta + \tau_0\frac{[1-e^{-m\dot\gamma}]}{\dot\gamma}\right)\dot\gamma, \tag{5}$$

where m is a parameter related to the transition between the solid and fluid regimes. The higher the value of m, the sharper the shape of the transition.

To non-dimensionalize the governing and constitutive equations, the following dimensionless variables are introduced:

$$y^* = \frac{y}{H}, \quad v^* = \frac{v}{V}, \quad t^* = \frac{t}{\rho H^2/\eta}, \quad \tau^* = \frac{\tau}{\eta V/H},$$

$$\gamma^* = \frac{\gamma}{V/H}, \quad p^* = \frac{p}{\eta V/H}, \quad Bn = \frac{\tau_0 H}{\eta V},$$

$$Re = \frac{\rho V H}{\eta}, \quad M = \frac{m}{H/V}, \quad b^* = \frac{b}{\eta V/H^2}, \tag{6}$$

where V is the reference velocity, H is the reference length, Re is the Reynolds number and Bn is the dimensionless Bingham number, a measurement of the yield stress relative to viscous stress. M is a dimensionless growth parameter. For convenience, the superscript star will be dropped in the following text. The non-dimensional governing and constitutive equations become:

$$\rho\frac{dv}{dt} = \nabla\cdot(-p\boldsymbol{I} + \tau) + \boldsymbol{b}, \tag{7}$$

$$\tau = \left\{1 + \frac{Bn[1-e^{-M\dot\gamma}]}{\dot\gamma}\right\}\dot\gamma. \tag{8}$$

3. Numerical method

The SPH method can be viewed as a numerical scheme in which the fluid flow is decomposed into discrete particles. Each of the particles has associated mass, density, velocity, and pressure. Using the information from the particles, the values of these variables at any location within the fluid can be interpolated. The SPH approach also removes the difficulties associated with convective terms and allows one to tackle fluid and solid flow problems involving large deformation and free surfaces in a relatively natural way.

3.1. Discretized SPH equations

The SPH method is based on the following integral

$$f(\mathbf{x}) \approx \int f(\mathbf{x}')\,W\left(\left|\mathbf{x}-\mathbf{x}'\right|,\ h\right)d\mathbf{x}', \tag{9}$$

where $f(\mathbf{x})$ is an arbitrary function, W is the weighting function, and h is a parameter that effectively controls the width of the weighting function with

$$\int W\left(\left|x-\mathbf{x}'\right|,h\right)d\mathbf{x}' = 1 \tag{10}$$

and the weighting function approaches the delta function as the parameter h approaches zero. Under such circumstance, the

approximate equal sign in Eq. (6) becomes strictly satisfied. The discretized SPH approximation can be written as

$$f(\mathbf{x}) \cong \sum_j \frac{m_j}{\rho_j} f_j W\left(\left|\mathbf{x}-\mathbf{x}'\right|, h\right), \tag{11}$$

where m_j and ρ_j are the mass and density corresponding to particle j, respectively. The discretized momentum equation can be written as:

$$\frac{dv_i^\alpha}{dt} = F_i^\alpha. \tag{12}$$

$$F_i^\alpha = \sum_j m_j \left(\frac{P_i^{\alpha\beta}}{\rho_i^2} + \frac{P_j^{\alpha\beta}}{\rho_j^2}\right) \nabla_i^\beta W_{ij} \tag{13}$$

where $W_{ij} = W\left(\left|\mathbf{x}_i - \mathbf{x}_j\right|, h\right)$. The subscript Roman indices indicate particles and the superscript Greek indices indicate spatial coordinates. W is a weight function which has the form:

$$W(r,h) = w_0 \begin{cases} \left(3-r/h\right)^5 - 6\left(2-r/h\right)^5 + 15\left(1-r/h\right)^5 & 0 \le r/h < 1 \\ \left(3-r/h\right)^5 - 6\left(2-r/h\right)^5 & 1 \le r/h < 2 \\ \left(3-r/h\right)^5 & 2 \le r/h < 3 \\ 0 & r/h \ge 3 \end{cases} \tag{14}$$

where $r = \left|\mathbf{r}_i - \mathbf{r}_j\right|$. When the normalization factor $w_0 = 7/(478\pi h^2)$, this weight function is quintic spline kernel for 2D simulation. The density could be obtained by integrating Eq. (1). However, the total mass is not exactly conserved. In the present study, following Ellero and Tanner [17], the following equation is obtained by replacing f_j with ρ_j in Eq. (11):

$$\rho_i = \sum_j m_j W\left(\left|\mathbf{r}_i - \mathbf{r}_j\right|, h\right). \tag{15}$$

Eq. (15) conserves the mass exactly. To evaluate the extra stress (Eq. (5)), one needs to define the discretized form of rate of deformation tensor:

$$\dot{\gamma}_i^{\alpha\beta} = k_i^{\alpha\beta} + k_i^{\beta\alpha} \tag{16}$$

where

$$k_i^{\alpha\beta} = \nabla^\beta V_i^\alpha \cong \sum_j \frac{m_j}{\rho_j}\left(V_j^\alpha - V_i^\alpha\right) \nabla^\beta W\left(\left|\mathbf{r}_i - \mathbf{r}_j\right|, h\right) \tag{17}$$

3.2. Artificial stress

In the SPH numerical simulation, when the material is in a state of tensile stress, the particle motion becomes unstable, leading to the so-called tensile instability [23,24]. This instability, which is strictly related to the interpolation technique of the standard SPH method, is especially noticeable when simulating the stretched state of a solid. As a consequence, particles tend to clump together and show unrealistic fracture-like behavior. To avoid this behavior, the artificial stress approach was adopted. The concept of artificial stress is to use a short-range repulsion force to prevent particles from getting too close; specifically, the artificial stress becomes effective when particle i is in tension and acts as a repulsion force avoiding particle clumping. Following Gray et al. [23], an additional artificial stress term was added in the parentheses of right side of Eq. (13):

$$\frac{P_i^{\alpha\beta}}{\rho_i^2} + \frac{P_j^{\alpha\beta}}{\rho_j^2} + \left(R_i^{\alpha\beta} + R_j^{\alpha\beta}\right)\left(\frac{W\left(\left|\mathbf{x}_i - \mathbf{x}_j\right|, h\right)}{W(d,h)}\right)^q, \tag{18}$$

where d is the mean initial distance between two neighboring particles and q is a parameter. The quantities $R_i^{\alpha\beta}$ and $R_j^{\alpha\beta}$ are assumed coaxial with the stress tensor [24]. The principal components of $R_i^{\alpha\beta}$ and $R_j^{\alpha\beta}$ are related to the principal stress components as follows:

$$\overline{R_i^\alpha} = -\varepsilon \frac{\overline{P_i^\alpha}}{\rho_i^2}, \quad \text{if } \overline{P_i^\alpha} > 0,$$

$$\overline{R_i^\alpha} = 0, \quad \text{if } \overline{P_i^\alpha} \le 0 \tag{19}$$

where $0 < \varepsilon < 1$ and $\overline{P_i^\alpha}$ is the principal stress component. A similar equation can be written for quantity $\overline{R_j^\alpha}$. The artificial stresses in the referenced coordinate system are then obtained by coordinate transformations. The artificial stress terms were used in the numerical simulations of the flow of Bingham fluids in the vane rheometer. Parameter d was chosen to be $1.11h$. For the weight function used in the present study (Eq. (14)), the ratio $W(0,h)/W(d,h)$ is 3.18. In the simulation we took parameter q equal to 4 following Monaghan [24]. Though Monaghan [24] also suggested that parameter ε takes a typical value of 0.2, the appropriate value of parameter ε depends on parameters h, q, and the number of spatial dimensions. By trial and error we found that ε equal to 0.5 successfully relieved the tensile instability in the simulation of flow of Bingham fluids in the vane rheometer.

3.3. Integration scheme

In the present study, a predictor–corrector scheme is used that offered second order accuracy in time. The particle accelerations $\mathbf{F}_i$ were computed via Eq. (18). The new fluid particle velocities and positions were found by a two-step integration:

$$\mathbf{r}_i(t+\Delta t) = \mathbf{r}_i(t) + \Delta t\, \mathbf{v}_i(t) + \frac{1}{2}\Delta t^2 \mathbf{F}_i(t), \tag{20}$$

$$\mathbf{v}_i\left(t + \frac{\Delta t}{2}\right) = \mathbf{v}_i(t) + \frac{\Delta t}{2}\mathbf{F}_i(t). \tag{21}$$

Once the predicted values of the independent variables were obtained for each fluid particle, the function $\mathbf{F}$ was evaluated using the predicted values in order to calculate the final corrected variables:

$$\mathbf{v}_i(t+\Delta t) = \mathbf{v}_i(t) + \frac{\Delta t}{2}\left(\mathbf{F}_i(t) + \mathbf{F}_i\left(t + \frac{\Delta t}{2}\right)\right). \tag{22}$$

To obtain a stable numerical solution, the time step Δt must satisfy the Courant–Friedrichs–Levy (CFL) condition [25], a constraint due to particle acceleration [26] and a constraint due to the viscous diffusion [25,27]:

$$\Delta t \le \frac{h}{3c}, \tag{23}$$

where c is the speed of sound,

$$\Delta t \le \min_i \left(\frac{h}{3\left|a_i\right|}\right), \tag{24}$$

where $\boldsymbol{a}_i$ is the acceleration of particle i, and

$$\Delta t \le \min_i \left(\frac{h^2}{2\upsilon_i}\right), \tag{25}$$

where $\upsilon_i = \eta_i/\rho_i$ is the kinematic viscosity of particle i.

3.4. State equation

In most SPH approaches, incompressible fluids are treated as slightly compressible fluids by employing an equation of state. In the current study, the following equation of state was adopted:

$$p(\rho) = c^2(\rho - \rho_0), \tag{26}$$

where ρ_0 is a reference density and c denotes the sound speed. The Mach number is defined by V/c, where V is a reference velocity. The density variation is proportional to the square of the Mach number. If a value is chosen corresponding to the real magnitude of the speed of sound of the fluid, then an extremely small time step has to be employed according to the Courant–Fredrich–Levy condition [25]. Monaghan [28] concluded that the sound speed could be artifically slowed for fluids without affecting the fluid motion too much. However, he also argued that the minimum sound speed should be around ten times greater than the maximum expected flow speeds. To make a proper choice of sound speed c that can yield the desired density variation (to simulate an ideal incompressible fluid) without losing computational efficiency, the sound speed was chosen following Monaghan [28] and Fang et al. [18] such that the density variation was confined within 1%. Usually the weak compressible assumption is used for SPH simulations of incompressible flows as adopted in the present approach. It is noted that new truly incompressible SPH formulations have been recently developed. For example, Cummins and Rudman [29] developed an SPH projection operator based on the solution of a pressure Poisson equation to solve a null divergence velocity field. Colin et al. [30] presented an SPH solution of the Helmholtz–Hodge decomposition for a null divergence velocity field in an incompressible fluid simulation. They also proposed a new version of the Laplacian formula for smoothing kernels. Instead of solving a pressure Poisson equation in order to get a divergence-free velocity field, Ellero et al. [31] achieved incompressibility by enforcing a kinematic constraint that the volume of the fluid particles is constant. Lagrangian multipliers were used to apply this restriction.

3.5. Boundary conditions

Throughout this paper, the flow fields considered were confined within solid boundaries over which a non-slip condition was applied. Numerous approaches have been proposed to handle the solid boundary conditions in SPH. In the repellent-particle approach [28], fixed boundary particles lie at the wall surfaces and exert an artificial repulsive force on approaching fluid particles to prevent them from penetrating the solid walls. The repellent-particle approach has greater flexibility in handling boundary conditions with complex geometry. However, problems arise if the particle density has to be evaluated near the wall: the density of those particles approaching the surface will decrease rapidly to about half the value of that in the bulk material. This causes a density gradient and consequently a substantial pressure gradient in the momentum equation which forces the particles to accelerate towards the wall producing loss of homogeneity in the dynamical grid and artificial layers parallel to the surface.

Another approach is the ghost-particle approach [9]. This considers the contribution of mirror boundary particles, which are created outside the domain simply by reflecting fluid particles across the boundary with opposite velocities. This approach has shown smooth behavior in modeling flows in less curved boundaries; however, it introduces numerical errors when dealing with curved solid surfaces.

For this study, Morris et al.'s [27] approach has been adopted. The solid material forming the boundary is filled with equi-spaced virtual boundary particles in a range of depth comparable with the support length scale of the weight function, whose velocity is deduced from those of the physical particles adjacent to the solid boundary. Boundary particles contribute to the usual SPH expressions for velocity, pressure and stress gradients. In this case, for every solid boundary particle j, a normal distance d_j to the boundary surface is defined. This is used to construct a tangent plane to the surface, and consequently the normal distance d_i to this plane for a selected fluid particle i. Finally, the velocity $\mathbf{v}_j$ of a solid particle, extrapolated across the tangent plane takes the form

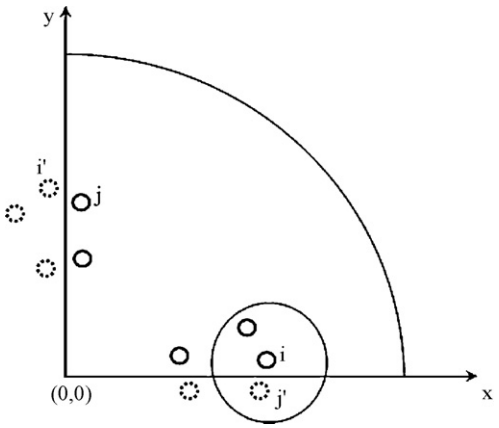

Fig. 1. Illustration of the application of periodic boundary conditions in a quadrant of the 2D vane rheometer.

$$\mathbf{v}_j = \mathbf{v}_i + \left(1 + \frac{d_j}{d_i}\right)(\mathbf{v}_w - \mathbf{v}_i), \tag{27}$$

where $\mathbf{v}_w$ is the wall velocity.

This approach allowed for the application of the non-slip boundary condition and resolution of the particle deficiency problem near the wall. Compared to the ghost-particle approach on curved solid surfaces, the present approach can handle curved interfaces since it does not introduce additional errors upon estimating the density of fluid particles that have neighbor particles within the solid boundaries. Specifically, the curved boundaries used in the present study are cylindrical walls of the vane and cylinder rheometers. In such cases, the normal of the tangential plane of a specific particle can be simply obtained by connecting the particle to the origin. For each boundary particle, the velocities are assigned via Eq. (27). Further, a new scheme was proposed in locating the fluid particles used in Eq. (27), that is: use the fluid particles whose distance to the tangential plane is close to that of the solid particle to the same plane. For example, if the distance from a solid particle to the tangential plane is within a range of $(0,h)$, then a fluid particle in the same distance range will be chosen to extrapolate the velocity of that solid particle. This method improves the accuracy of the computational results when dealing with curved boundaries.

In the present study, numerical simulations in vane and coaxial cylinder rheometers were performed. Taking advantage of symmetry, a domain which is a quarter of the original one was adopted for computational efficiency. As a consequence, periodic boundary conditions have to be applied in the θ (rotational) direction. That is to say, when the computation is carried out for particles situated within a range of 3 h to the plane $\theta = 0 (\theta = \pi/2)$, the particles close to the plane $\theta = \pi/2 (\theta = 0)$ are also considered as potential neighbors. For example, to compute the properties of a given particle (i, see Fig. 1) close to the plane $\theta = 0$, the coordinates, velocity and stresses of its neighbor particle j' close to plane $\theta = \pi/2$ are transformed to the current reference frame. Specifically,

$$x_{j'} = y_j, \quad y_{j'} = -x_j, \quad v^x_{j'} = v^y_j, \quad v^y_{j'} = -v^x_j, \quad \tau^{xx}_{j'} = \tau^{yy}_j,$$
$$\tau^{yy}_{j'} = -\tau^{xx}_j, \quad \tau^{xy}_{j'} = \tau^{xy}_j. \tag{28}$$

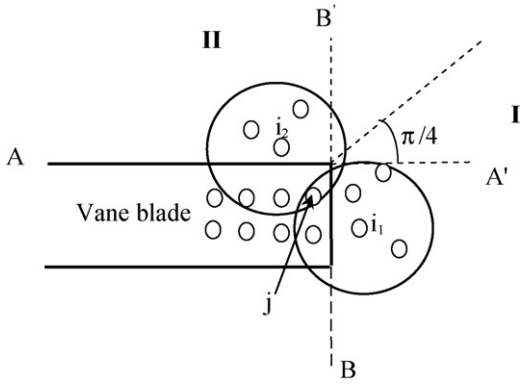

Fig. 2. Illustration of the application of boundary conditions at the surface of a vane blade.

If particle i is originally situated close to plane $\theta = \pi/2$ while its neighbor is located close to the plane $\theta = 0$, the transformation will instead take the form

$$x_{j'} = -y_j, \quad y_{j'} = x_j, \quad v^x_{j'} = -v^y_j, \quad v^y_{j'} = v^x_j,$$
$$\tau^{xx}_{j'} = -\tau^{yy}_j, \quad \tau^{yy}_{j'} = \tau^{xx}_j, \quad \tau^{xy}_{j'} = \tau^{xy}_j. \tag{29}$$

To assess the flow properties of the fluid particles close to the tips of the vane blades, additional consideration is needed to deal with the geometric singularity. A single solid particle can have fluid particle neighbors across an abruptly changing interface. As shown in Fig. 2, if a straight line is drawn between the solid particle j and fluid particle i_1, this will cross the plane $y - y'$, while the line connecting particle j to particle i_2 will cross the plane $x - x'$. Under such circumstances, we propose the concept of multiple flow properties for solid boundary particles. Depending on the location of the fluid particle being assessed, different flow properties can be applied to one specific solid boundary particle. For example, in the case shown in Fig. 2, when a computation is performed involving fluid particle i_1, which is situated in regime *I*, the reference plane $y - y'$ is chosen to assess the velocity of the boundary particle j, the $x - x'$ plane is used as a reference plane when a computation is conducted involving particle i_2 located in regime *II*. Since different reference planes are used for these two cases, the flow properties assigned to the solid particle j can be different. This approach helps resolve the singularity problem in applying the boundary conditions at the tips of the vane blades, and it proves effective in providing smoothed solutions in the numerical simulation.

3.6. Rotating non-inertial reference frame

A two-dimensional vane geometry was used in the present study. To handle the complex boundary condition at the surface of the vane blades, the flow field was solved in a non-inertial reference frame, which rotates with the inner cylinder or vane blades at a angular velocity ω. Assuming a constant angular velocity, the momentum equation can be rewritten in the rotating non-inertial reference frame as

$$\rho\left[\frac{d\boldsymbol{v}}{dt} + 2\omega \times v + \omega \times (\omega \times r)\right] = \nabla \cdot \boldsymbol{P} + \boldsymbol{b}. \tag{30}$$

On the left side, the terms $2\omega \times \boldsymbol{v}$ and $\omega \times (\omega \times r)$ correspond to the Coriolis and centrifugal forces, respectively. Since there are no derivative terms involved in the Coriolis and centrifugal accelerations, there are no additional difficulties in solving Eq. (30).

4. Validation of the numerical scheme

In this section, the SPH algorithm is validated by comparing the numerical results for the Poiseuille flow of Bingham fluids and the tangential angular flow of Newtonian fluids with analytical solutions.

4.1. Poiseuille flow

A numerical simulation was performed for the flow in a two-dimensional channel. In a rectangular simulation box, a total number of 2500 particles were used. Periodic boundary conditions were imposed in the x-direction (flow direction) with particles leaving the right side re-inserted on the left side with the same velocity and y coordinate. In addition, rigid boundary conditions are considered at the upper and lower plates, which consist of a thick region filled with boundary particles entering in the interpolation process and interacting with the fluid particles. The velocities of the solid boundary particles are extrapolated via Eq. (27).

The non-dimensional governing and constitutive equations for the Poiseuille flow of Bingham fluids can be written as:

$$\frac{\partial v^x}{\partial t} = \frac{\partial \tau^{yx}}{\partial y} + b, \tag{31}$$

$$\tau^{yx} = \left\{1 + \frac{Bn[1 - e^{-M\dot{\gamma}}]}{\dot{\gamma}}\right\}\frac{\partial v^x}{\partial y}. \tag{32}$$

The exact steady state solution for the Poiseuille flow of Bingham fluids (non-regularized model) can be solved analytically:

$$v^x = \frac{1}{2}b\left(\frac{1}{4} - y^2\right) - Bn\left(\frac{1}{2} - y\right) \quad \frac{1}{2} \geq y \geq y_0$$

$$v^x = \frac{1}{2}b\left(\frac{1}{2} - y_0\right)^2 \quad 0 \leq y < y_0, \tag{33}$$

where $y_0 = Bn/b$ and for convenience the non-dimensional pressure gradient b is assigned to be equal to one. The analytical solution (Eq. (33)) is valid for $0 \leq y \leq 1/2$ and is symmetric with respect to the y-axis. A parametric study was performed by setting $Bn = 0$ (Newtonian fluid), 0.1, 0.2 and 0.3, and the numerical results are compared with the analytical solution (Eq. (33)). In the simulation sound speed c takes a value of 10. That is to say, quantity c^2 is equal to 100. Considering that the reference velocity is equal to 0.125, the density variation can be well confined within 1%.

Fig. 3 shows the computed velocity profiles for the Poiseuille flow of Bingham fluids with different Bingham number, i.e. 0 (Newtonian fluid), 0.1, 0.2 and 0.3, respectively. The simulation results are in good quantitative agreement with the analytical solutions (Eq. (33)), which are also presented. The computed stresses are shown in Fig. 4 along with the analytical values. Actually, the analytical shear stress is a straight line ranging from −0.5 to 0.5 and the numerical results compare well with the theoretical values. It is noted that the dimensionless growth parameter M was chosen to be 500. As discussed in the work of Chatzimina et al. [32]: beyond a critical Bn value, further increasing of the growth parameter M will cause the requirement of much smaller time step and lead to higher accumulated round-off errors. In the present study we found that a growth parameter value of 500 gave close results compared to the exact solution (Fig. 3).

4.2. Tangential angular flow of Newtonian fluids

In this section, we report on numerical simulations that were performed to determine the velocity and stress distributions for the tangential flow of an incompressible Newtonian fluid between

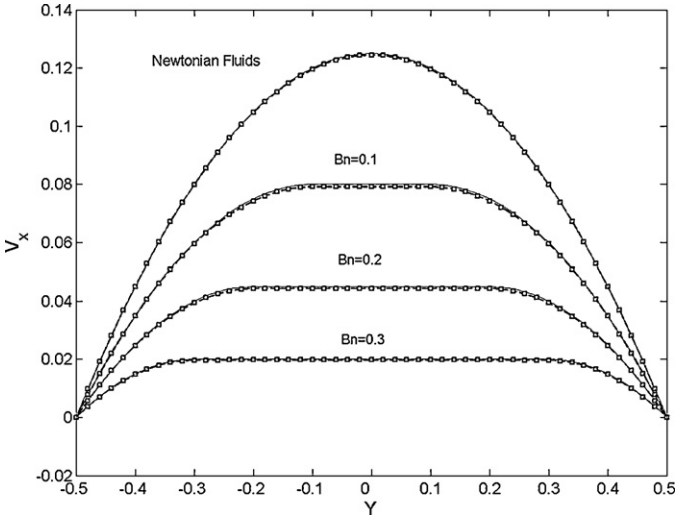

Fig. 3. Velocity profiles for Poiseuille flow of Bingham fluids with different yield stress. (—: numerical result, –□–: analytical solution).

two coaxial cylinders. The outer cylinder was rotating at an angular velocity ω_0 while the inner one was fixed. The end effects were neglected and the problem was treated as a two-dimensional one. In steady laminar flow, the fluid moved in a circular pattern and the only non-trivial component of velocity is the one in the angular direction. The momentum equation (steady state) and the boundary conditions can be written in cylindrical coordinates [33] as:

$$0 = \frac{d}{dr}\left(\frac{1}{r}\frac{d}{dr}(rv^{\theta})\right), \tag{34}$$

$$v^{\theta} = 0 \quad \text{at } r = \kappa R, \tag{35}$$

$$v^{\theta} = \omega_0 R \quad \text{at } r = R, \tag{36}$$

where κ is equal to 0.512 and parameter θ denotes the angular direction. Solving Eq. (34), combined with boundary conditions (Eqs. (35) and (36)), yields the analytical solution for the velocity:

$$v^{\theta} = \omega_0 R \frac{((\kappa R/r) - (r/\kappa R))}{(\kappa - (1/\kappa))}. \tag{37}$$

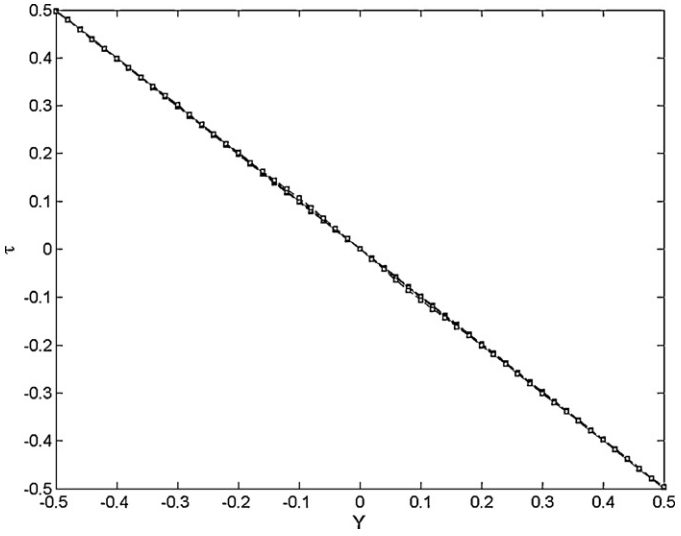

Fig. 4. Shear stress profiles for Poiseuille flow of Bingham fluids with different yield stress. (—: numerical result, –□–: analytical solution).

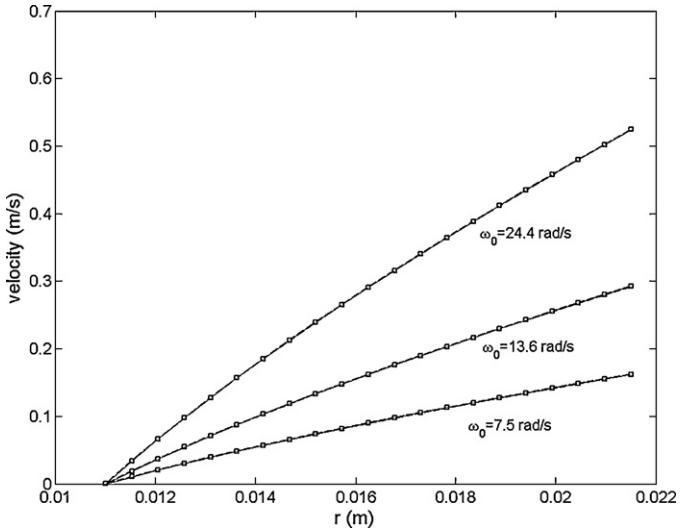

Fig. 5. Comparison of velocity profiles in the tangential angular flow of Newtonian fluids at three different angular velocities (—: numerical result, –□–: analytical solution).

The shear stress distribution is:

$$\tau^{r\theta} = -\eta\omega_0 R^2 \left(\frac{1}{r^2}\right)\left(\frac{\kappa^2}{1-\kappa^2}\right) \tag{38}$$

In the numerical simulation, the radii of the inner and the outer cylinders were 11 and 21.5 mm, respectively. The plastic viscosity of the fluid was 27.5 Pa s (the same value is used in the remaining of the text). Three simulations were performed with different angular velocities, i.e. 7.5, 13.6 and 24.4 rad/s (1.20, 2.17 and 3.88 rps, respectively). The dimensions of the cylinder, the viscosity of the fluid and the angular velocities were chosen according to an actual experiment, for which the details are presented in the following section. The computation was performed in a two-dimensional domain by using 4286 SPH particles. Non-slip boundary conditions were applied to the outer and inner surfaces. 412 solid boundary particles filled a region close to the outer surface, while 202 solid particles filled the region close to the inner surface. At the $x-x'$ and $y-y'$ planes, periodic boundary conditions were imposed with particles leaving the $x-x'$ plane re-entering the $y-y'$ plane with velocities and coordinates computed via Eqs. ((28) and (29)).

Figs. 5 and 6 show the comparison of the numerical results and analytical solutions for the tangential angular flow of Newtonian fluids with three different angular velocities. It can be observed from Fig. 5 that the computed velocities almost coincide with the theoretical values. Overall, the numerical results for shear stress are in good agreement with the analytical values except for slightly lower values of stress close to the inner wall, as seen in Fig. 6. The maximum relative error at the inner wall is about 1.6%, and about 0.9% at the outer wall, which means the accuracy of the present approach is acceptable. It is noted that Chatzimina et al. recently showed that the error in the computed wall shear rate and hence shear stress depends on the diameter ratio and material parameters [34].

5. Comparison of numerical predictions and experimental results

5.1. Experimental set-up and results

The main reason for the experimental measurements was to provide data to validate the SPH model. A shear rate-controlled coaxial cylinder and a vane rheometer were used. Both rheometers

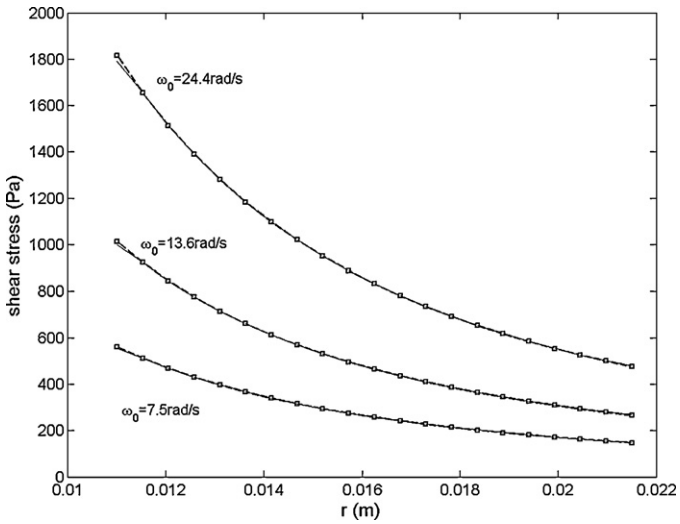

Fig. 6. Comparison of the shear stress in the tangential angular flow of Newtonian fluids at different angular velocities (—: numerical result, –□–: analytical solution).

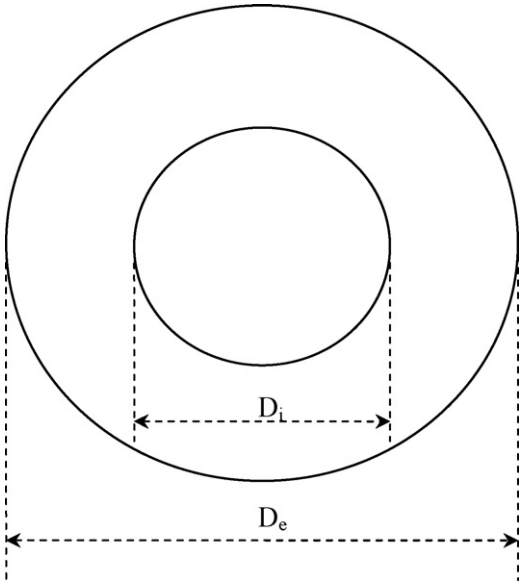

Fig. 7. Illustration of the 2D profile of the coaxial cylinder rheometer (D_i: inner diameter 22 mm; D_e: outer diameter 43 mm).

used the same outer cylindrical container with a diameter 43 mm. The torque resulting from the material resistance was measured at the central rotating tools. Two types of corresponding tools were used: (i) a rotor cylinder (Fig. 7) and (ii) a cross vane (Fig. 8). Both tools had the same length (16 mm) and the same diameter (22 mm). The rotor had smooth walls as is customary in a coaxial cylinder rheometer.

The fluid used was a standard silicone based oil.[1] The nominal viscosity of the oil was 27.5 Pa·s at room temperature as given by the manufacturer. To verify the operation of the rheometer, the viscosity of the oil was measured using a standard coaxial cylinder rheometer with a gap of 2.5 mm (inner cylinder diameter 38 mm and container 43 mm) and found to be 26.9 Pa·s. This implies an

[1] A standard oil from Cannon named S8000 was used. Commercial equipment, instruments, and materials mentioned in this report are identified to foster understanding. Such identification does not imply recommendation or endorsement by the National Institute of Standards and Technology (NIST), nor does it imply that the materials or equipment identified are necessarily the best available for the purpose.

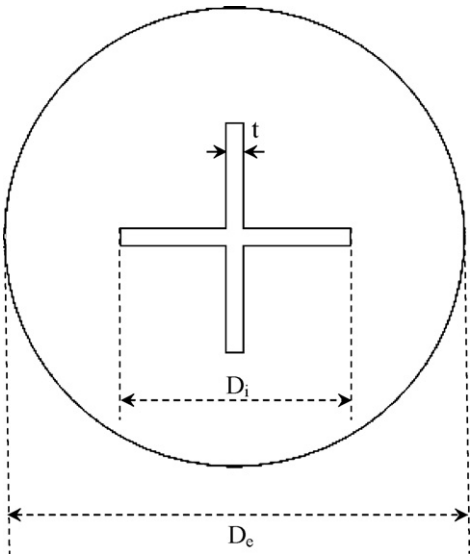

Fig. 8. Illustration of the 2D profile of the vane rheometer (D_i: length of the vane blade 22 mm; D_e: outer diameter 43 mm; t: thickness of the vane blade 1.1 mm).

Table 1
Experimental data for the measured torques (Newtonian fluids).

Angular velocity rad/s (rps)	7.5 (1.20)	13.6 (2.17)	24.4 (3.88)
Torque for rotor (10^{-6} Nm)	15,600	27,100	47,900
Torque for vane (10^{-6} Nm)	11,800	20,900	37,600
Ratio of the torque (vane over rotor data)	0.756	0.771	0.785

error of 2% with the nominal value at the same temperature. The reproducibility of the measurements was 0.3%. It is noted that for the experiment with vane and coaxial cylinder rheometers, the outer walls were fixed, since in the simulations the outer boundary rotated.

Table 1 shows the experimental data obtained with both tools at three different angular velocities. Fig. 9 shows more experimental data under different angular velocities.

From Table 1, the measured torques with the vane were about 0.75–0.79 of those measured via the rotor attachment. The trend is that the ratio of the vane torque to the rotor torque increases with the angular velocity of the tool. If the assumption that the vane could be approximated by a virtual cylindrical surface is correct, then the two values should be identical. No slippage at the surface of the cylindrical rotor is occurring. Actually, the torque

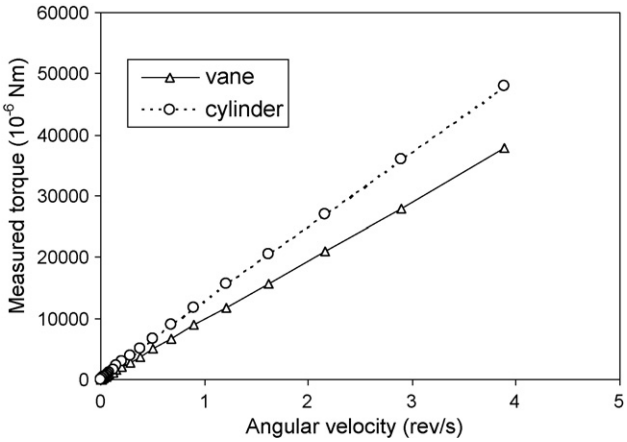

Fig. 9. Experimental data for the torques measured for the vane and rotor rheometers at different angular velocities.

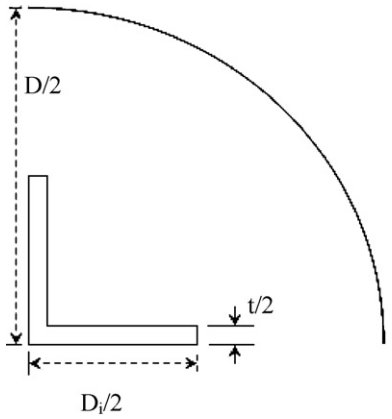

Fig. 10. Illustration of a quarter part of the 2D vane rheometer.

values measured with the rotor are higher than those measured with the vane, implying that secondary flow might be occurring within the vane. Atkinson and Sherwood [35] showed that in an unbounded Newtonian fluid, a n-bladed 2D vane will have a torque that is smaller by a factor close to $1-(1/n)$ (0.75 when $n=4$) than that for a coaxial cylinder at zero Reynolds number. Our results are within the range of 75–79%. Considering the fact that in Atkinson and Sherwood's work [35], the flow is Stokes flow without the consideration an inertia terms, the blades used in their study have zero thickness instead of a finite value, and the media is infinitely large, we consider this deviation to be acceptable.

5.2. Comparison between experimental data and simulation

The computational domain for the 2D coaxial cylinder rheometer is the same as that in Section 4.2. For the computations involving the 2D vane rheometer (see Fig. 10), 5637 fluid SPH particles were used. No-slip boundary conditions were applied to the outer wall surfaces: 412 solid boundary particles filled in a region adjacent to the outer surface. In addition, the vane blades were represented by 172 solid particles, and the newly proposed scheme introduced in Section 3.5 was employed to deal with the boundary conditions at the tips of the vane blades. In order to study the convergence properties, a computation was also carried out with higher density of particles (22550 fluid SPH particles, 818 solid boundary particles and 688 solid particles) for the flow of a Newtonian fluid in the vane rheometer at an angular velocity of 7.5 rad/s. The obtained average shear stresses on the surface of the outer cylinder is 105.9 Pa.

Table 2
Computational results for the shear stresses on the outer surface of the rheometers (Newtonian fluids).

Angular velocity rad/s	7.5	13.6	24.4
Stress (Pa)/non-dimensional stress for cylinder rheometer	149.4/0.724	267.7/0.716	479.0/0.714
Stress (Pa)/non-dimensional stress for vane rheometer	105.6/0.512	195.3/0.522	351.5/0.524
Ratio of the shear stresses (vane over rotor data)	0.707	0.730	0.734

The relatively error is about 0.28% compared to the 105.6 Pa stress obtained using 5637 fluid SPH particles. We conclude that using 5637 fluid SPH particles achieves satisfactory results for the present numerical simulation. It is also noted that to confine the density variation within a range of 1%, we chose the square of sound speed, c^2, to be 1000 in the simulations of the fluid flow in vane and coaxial cylinder rheometers.

For both the vane and the coaxial cylinder rheometers, the outer walls were fixed while the vane and the rotor were rotating with three different angular velocities. To take into account the complex boundary conditions at the surface of the vane blades, the numerical simulation was performed in a rotating non-inertial reference frame. Under such circumstances, the boundary conditions needed to be modified by fixing the inner vane or cylinder rotors while rotating the outer cylindrical walls. Table 2 shows the corresponding results from the 2D simulation. The average shear stresses on the surfaces of the outer cylinders of both the cylinder and vane rheometers and their ratios are presented in this table. Compared to the stress ratios from the experimental data, the computed values are 5.2–6.5% lower. It is noted that a 2D vane is considered here, and not a 3D one, as is the case associated with the experimental data. The vane was assumed to be long enough so that the shape and position of the shearing surface was independent of the shear stress profile near the upper and lower ends. Obviously, the end effect problem associated with the contributions of the applied torque on these upper and lower end surfaces cannot be completely resolved without the help of a 3D numerical simulation. Savamand et al. studied Bingham fluids in a 3D vane rheometer by means of finite element simulation [36]. But the applied outer wall angular velocity in their study is much smaller (1.05 rps) compared to those in the present study. Nevertheless, the relative error between the experimental and the present 2D simulation results is about 6%, which is considered acceptable especially taking into consideration that the simulation is in 2D.

Table 3
Computational results for the shear stress ratios on the outer surfaces of the rheometers.

Angular velocity (rad/s)	Reynolds number (Re)	Yield stress (Pa)	Bingham number (Bn)	Non-dimensional shear stress at the outer surface of vane rheometer	Ratio of the stress at the outer wall (vane data over cylinder data)
7.5	0.13	0	0	0.512	0.707
		137.5	0.67	0.797	0.766
		275.0	1.33	1.129	0.831
		412.5	2.0	1.427	0.886
13.6	0.23	0	0	0.52	0.730
		137.5	0.37	0.677	0.758
		275.0	0.74	0.841	0.785
		412.5	1.10	1.012	0.809
		550.0	1.47	1.175	0.836
		687.5	1.84	1.348	0.863
24.4	0.41	0	0	0.52	0.734
		137.5	0.20	0.628	0.771
		275.0	0.41	0.722	0.791
		412.5	0.61	0.813	0.803
		825.0	1.23	1.09	0.834
		1237.5	1.84	1.333	0.857

6. A parametric study for flow of Bingham-like fluids with different yield stresses and applied angular velocities

A parametric study for Bingham-like fluids with different yield stress values was performed. This study allowed for the investigation of the impact of the yield stress on the flow properties in the 2D rheometers using the two geometries (rotor and vane). The computational domain for the 2D rotor and vane rheometer was the same as that in Sections 3 and 4. The Dimensionless Bingham number for different flow cases was computed based on the reference length H, the reference velocity V and the viscosity, η. The viscosity has a value of 27.5 Pa. The reference length H was chosen to be the radius of the outer cylinder, i.e. 0.0215 m. The reference velocity for each case was chosen as the velocity of the rotating outer cylinder. The yield stresses used to compute the Bingham numbers are listed in the second column of Table 3. These values were chosen on the basis of typical yield stress values of concrete and mortar mixtures [37]. The smallest Bingham number is 0.2 for the flow in vane and cylinder rheometers (Table 3). Chatzimina et al. [32] had a detailed discussion on the effect of the growth parameter M (Eq. (8)) on the flow field of Bingham fluids. They concluded that for moderate or high Bingham number the results are not very sensitive to the growth parameter M. In the present study the dimensionless growth parameter M was chosen to be 500 for the simulation of flow in vane and coaxial cylinder rheometers.

Table 3 shows the computational results of non-dimensional shear stress on the outer cylinder surface of the vane rheometer for the flow of Bingham fluids with different yield stress under different applied angular velocities. The fourth column of Table 3 shows the ratios of non-dimensional shear stress on the outer cylinder surface of the 2D vane rheometer to that from the coaxial cylinder rheometer. We observe that the stress ratios between the vane and coaxial rheometers are always less than one, since the fluid between the vane blades dissipates part of the input energy and hence decreases the torque transmitted to the outer wall. This effect eventually causes lower shear stress values (or torques in the experiment) obtained at the outer wall for the vane rheometer compared to that obtained for the coaxial cylinder rheometer.

The stress ratios versus Bingham numbers under different applied angular velocities are illustrated in Fig. 11. It is observed that the higher the Bingham number, the larger the ratio of non-dimensional shear stress from the vane rheometer to that from the coaxial cylinder rheometer, regardless of the magnitude of the angular velocity applied to the outer cylinder. On the other hand, the applied angular velocity also plays a non-negligible role in determining the stress ratios between the vane and coaxial cylinder rheometers. Specifically, for smaller Bingham numbers (<1), the shear stress ratio is higher at higher magnitudes of applied angular velocities; for larger Bingham numbers (>1.5), the shear stress ratio is lower at higher magnitude of applied angular velocities; while for Bingham numbers within the range of 1–1.5, the shear stress ratios between the vane and coaxial cylinder rheometers are quite close. As the magnitude of the applied angular velocity increases, the inertial force becomes more prominent relative to the viscous force. As shown in Table 3, the Reynolds number varies from 0.13 to 0.41 for as the applied angular velocity increases from 7.5 to 24.4 rad/s. This possibly contributes to the small variation of stress ratios under different applied angular velocities.

The Bingham number is a measure of the ratio of the yield stress to the viscous stress. Note that for a vane rheometer, the size of the unyielded region in the inner blade region is larger for flow with higher values of the Bingham number; consequently the flow field in the vane rheometer is closer to that in a coaxial cylinder rheometer, which leads to a higher shear stress ratio between the vane and coaxial cylinder rheometers. In the case where the applied angular velocity is 7.5 rad/s, the stress ratio increases from about 0.77 for the lower yield stress case (Bn = 0.67) to about 0.89 for the

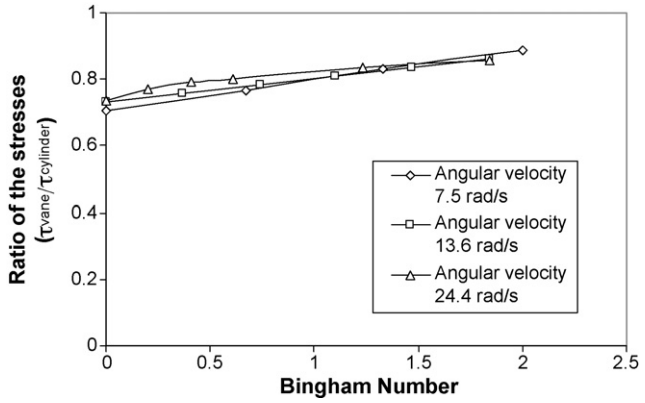

Fig. 11. Ratio of non-dimensional shear stress on the outer cylinder surface of a 2D vane rheometer to that of a coaxial cylinder rheometer for the flow of Bingham fluids with different Bingham numbers at different angular velocities.

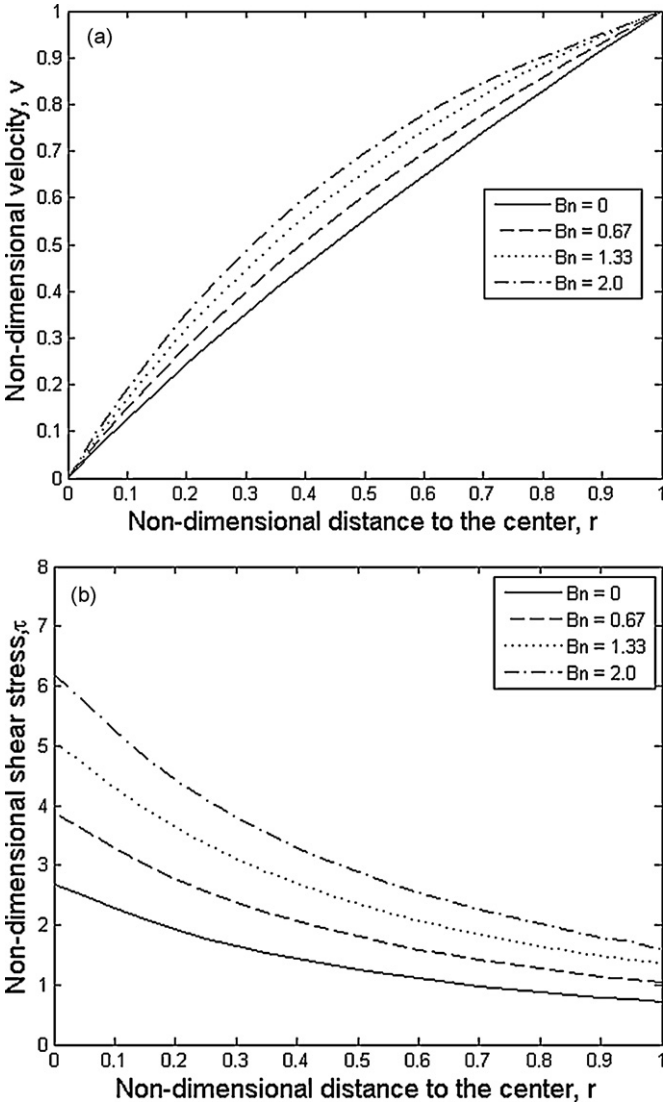

Fig. 12. (a) Non-dimensional velocity profiles for the flow of Bingham fluids with different Bingham numbers in a 2D coaxial cylinder rheometer (angular velocity: 7.5 rad/s). (b) Non-dimensional shear stress profiles for the flow of Bingham fluids with different Bingham number in a 2D coaxial cylinder rheometer (angular velocity: 7.5 rad/s).

larger yield stress case ($Bn = 2.0$). In addition, the shear stress ratio is monotonically increased with the Bingham number for different applied angular velocities, but the slope of stress ratio versus Bingham number curves are slightly different. For smaller magnitude of applied angular velocity the slope is higher than that for a larger applied angular velocity. For the cases with an angular velocity of 7.5 or 13.6 rad/s, the curves are close to a straight line; while for the case with an angular velocity of 24.4 rad/s, the stress ratio versus Bingham number curve tends to flatten out when the Bingham number is greater than 0.61.

Figs. 12–14 show the numerical results for the flow of Bingham fluids under different applied angular velocities in a 2D coaxial cylinder rheometer. Specifically, Figs. 12a, 13a and 14a show the computed non-dimensional velocity profiles under different applied angular velocities of 7.5, 13.6 and 24.4 rad/s. Figs. 12b, 13b and 14b show the corresponding non-dimensional effective shear stress profiles. Note that this effective shear stress is defined as $\tau = (1/2)\sqrt{\tau' : \tau'}$, where τ' is the non-dimensional traceless extra stress tensor. The Bingham numbers used in different cases varied from 0.0 to 2.0. It is observed that at a fixed angular velocity, higher shear stress is obtained for fluids with higher Bingham number. In all cases, the material between the two cylinders was flowing, i.e. no unyielded areas were observed.

Figs. 15 and 16 present the numerical results for the flow of Bingham fluids with different Bingham numbers under an applied angular velocity of 7.5 rad/s in a 2D vane rheometer. Specifically, Figs. 15a and 16a illustrate the contour plots of the non-dimensional velocity for Bingham fluids with Bingham numbers of 0.67 and 2.0, and Figs. 15b and 16b show the corresponding streamlines near the vane blade tips. These streamline plots are drawn in the Eulerian reference frame. It can be observed that the fluids close to the tip of the vane blade do not move along the concentric lines. That is to say, there is no clear circular surface that can be defined as streamlines for this flow. We can also observe that streamlines are closer to the concentric lines if they are farther away from the vane blade tip. In addition, for the flow with a higher Bingham number of 2.0 (Fig. 16b) the streamlines are closer to the concentric line than those in the flow with a lower Bingham number of 0.67 (Fig. 15b). This makes sense because in a flow with a higher Bingham number, there will be larger unyielded zones between the two vane blades; in other words, larger amount of fluids in the inner blade region tends to move with the blades in a flow with higher Bingham numbers.

From the contour plots of the normalized non-dimensional stress distribution (Figs. 15c and 16c), we can observe stress concentrates at the tips of the vane blade (Figs. 15d and 16d), as a result of non-uniform flow around the blade tips. The maximum effective shear stress is located close to the center of the vane blade tip surface facing to the outer cylinder wall, at which a maximum shear rate occurs (note that for symmetry we only show half of the vane

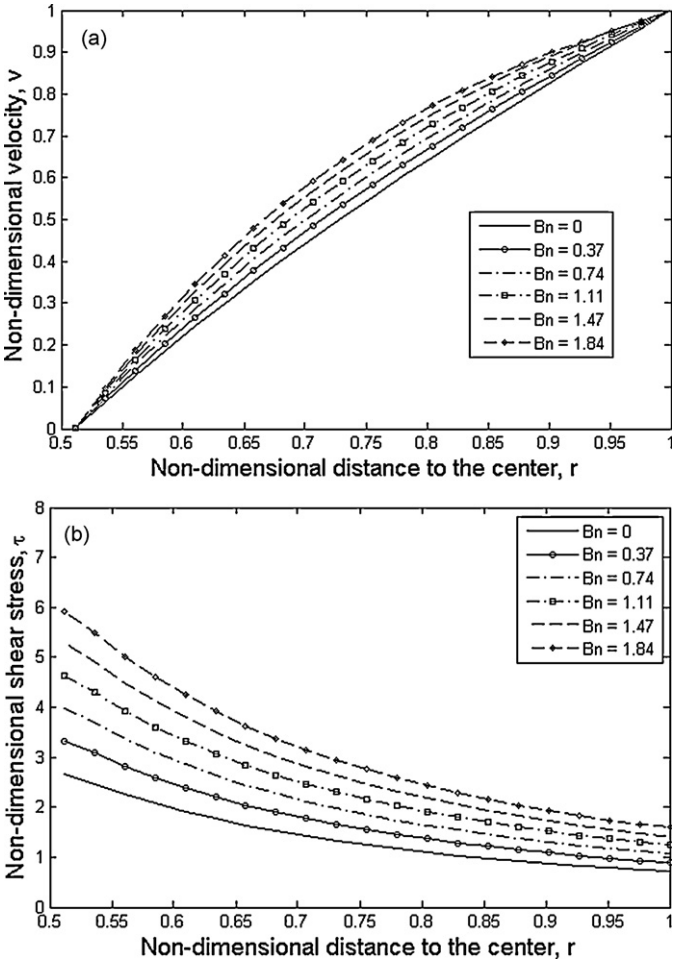

Fig. 13. (a) Non-dimensional velocity profiles for the flow of Bingham fluids with different Bingham numbers in a 2D coaxial cylinder rheometer (angular velocity: 13.6 rad/s). (b) Non-dimensional shear stress profiles for the flow of Bingham fluids with different Bingham numbers in a 2D coaxial cylinder rheometer (angular velocity: 13.6 rad/s).

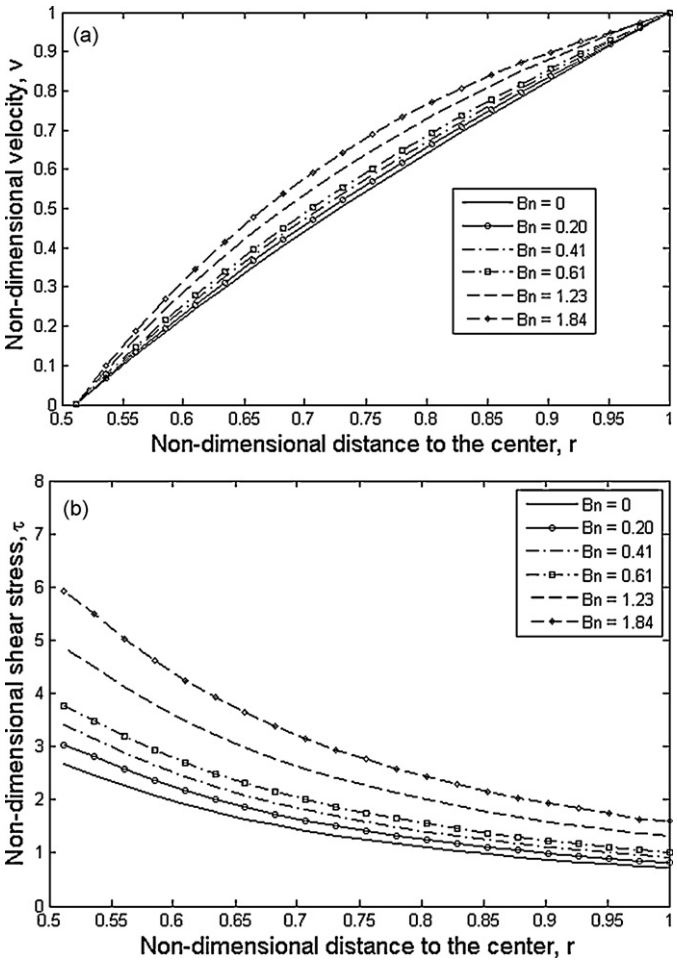

Fig. 14. (a) Non-dimensional velocity profiles for the flow of Bingham fluids with different Bingham numbers in a 2D coaxial cylinder rheometer (angular velocity: 24.4 rad/s). (b) Non-dimensional shear stress profiles for the flow of Bingham fluids with different Bingham numbers in a 2D coaxial cylinder rheometer (angular velocity: 24.4 rad/s).

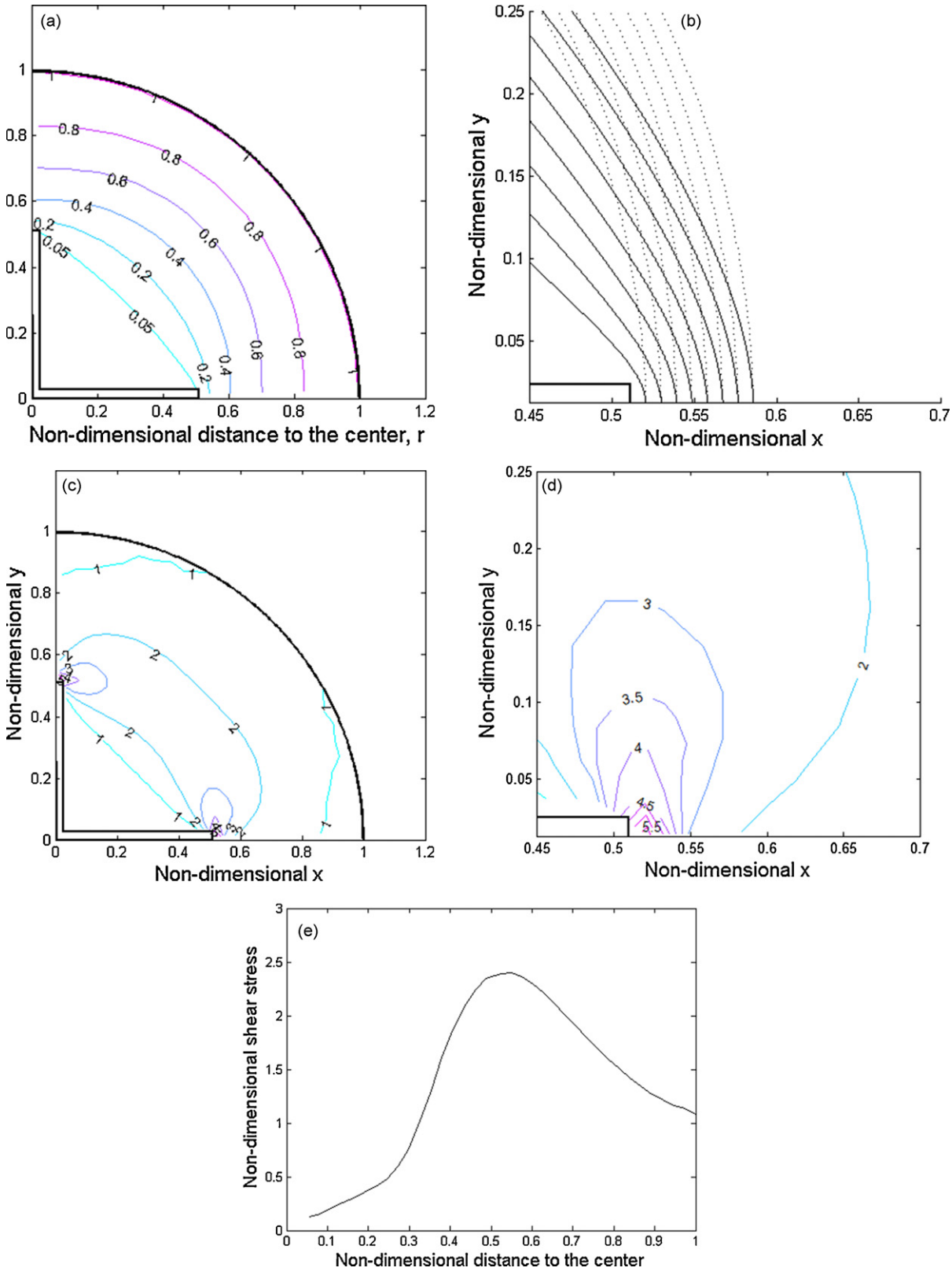

Fig. 15. (a) Contour plot of non-dimensional velocity for a Bingham fluid with a Bingham number of 0.67 in a vane rheometer (angular velocity: 7.5 rad/s). (b) Streamlines near the vane blade tip for Bingham fluid with a Bingham number of 0.67 in a 2D vane rheometer (angular velocity: 7.5 rad/s). (c) Contour plot of normalized non-dimensional shear stress for Bingham fluid with a Bingham number of 0.67 in vane rheometer (angular velocity: 7.5 rad/s). (d) Zoomed contour plot of normalized non-dimensional shear stress (by Bingham number 0.67) near the vane blade tip for Bingham fluid with a Bingham number of 0.67 in a vane rheometer (angular velocity: 7.5 rad/s). (e) Normalized non-dimensional shear stress (by Bingham number 0.67) profile along the line $\pi/2$ in vane rheometer (Bingham number 0.67, angular velocity: 7.5 rad/s).

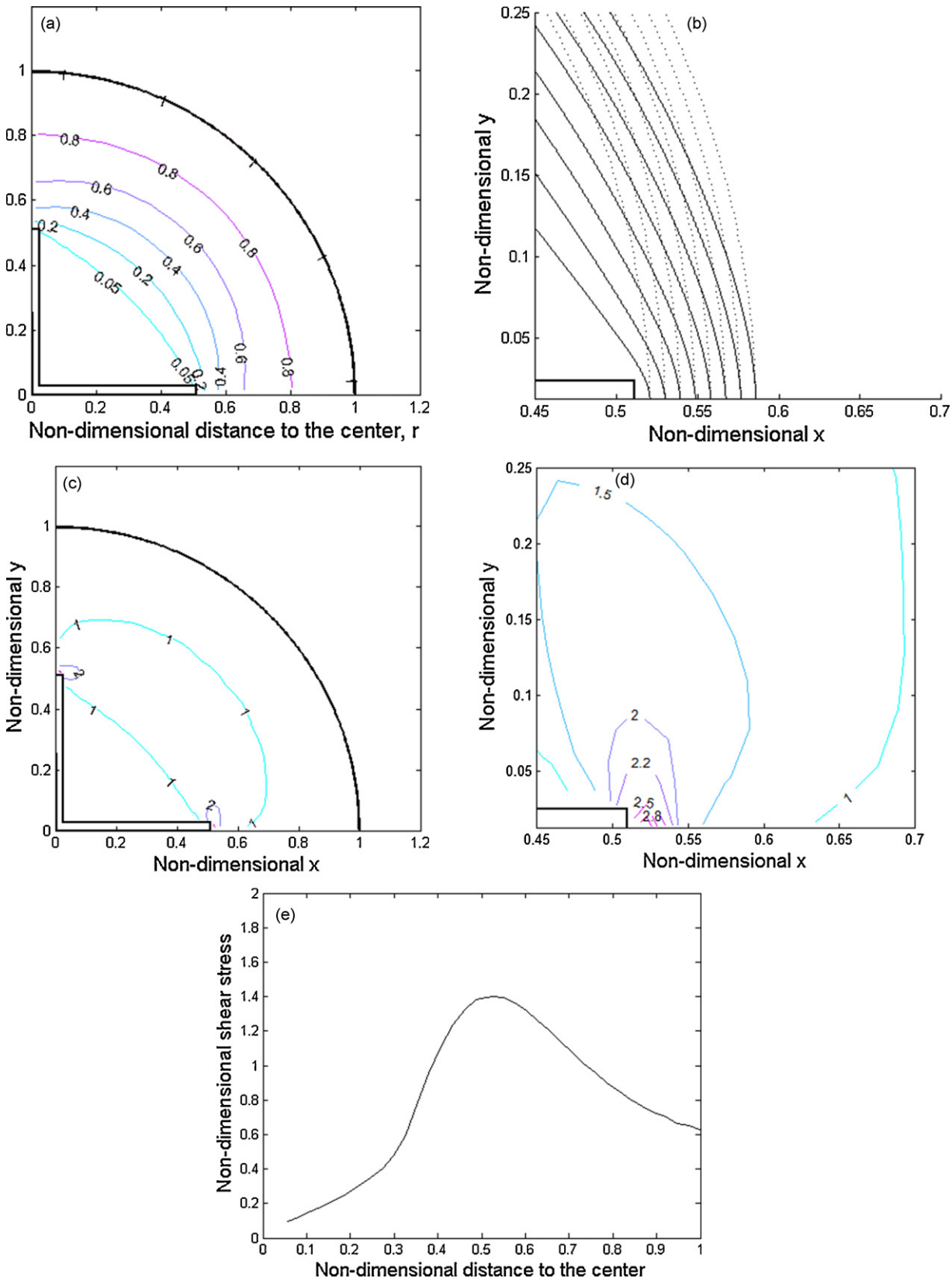

Fig. 16. (a) Contour plot of non-dimensional velocity for a Bingham fluid with a Bingham number of 2.0 in vane rheometer (angular velocity: 7.5 rad/s). (b) Streamlines near the vane blade tip for Bingham fluid with a Bingham number of 2.0 in a 2D vane rheometer (angular velocity: 7.5 rad/s). (c) Contour plot of normalized non-dimensional shear stress (by Bingham number 2.0) for Bingham fluid with a Bingham number of 2.0 in vane rheometer (angular velocity: 7.5 rad/s). (d) Zoomed contour plot of normalized non-dimensional shear stress (by Bingham number 2.0) near the vane blade tip for Bingham fluid with a Bingham number of 2.0 in vane rheometer (angular velocity: 7.5 rad/s). (e) Normalized non-dimensional shear stress (by Bingham number 2.0) profile along the line $\pi/2$ in a vane rheometer (angular velocity: 7.5 rad/s).

blade). The non-dimensional stresses shown are normalized by the Bingham number to better reveal which part of the fluid is yielded or unyielded, since the normalized dimensionless stress is equal to τ/τ_0. The interface between the flow and unyielded areas can be distinguished by the stress lines with a value of $\tau/\tau_0 = 1$: the material is yielded when $\tau/\tau_0 > 1$ and it is unyielded when $\tau/\tau_0 < 1$. Comparing the numerical results for flows with different Bingham numbers at a fixed applied angular velocities (Figs. 15c and 16c) we can see that a higher Bingham number leads to a larger size of unyielded regions in the inner vane blades region and in the neighbor area of the outer cylindrical wall.

Figs. 15c and 16c also show that there are regions close to the outer cylinder wall that remain unyielded ($\tau/\tau_0 \leq 1$). For the lower Bingham number case ($Bn = 0.67$, Fig. 15c), the two unyielded regions are located close and the x and y axes defined by the horizontal and vertical vane blades. For the case with a larger Bingham number of 2.0 (Fig. 16c), the unyielded regions close to the outer wall are connected. This result is in agreement with the observation of Landry et al.: "*for sufficiently large yield stress all basic flows have unyielded fluid layer attached to the outer wall*" [38]. In the region close to the x and y axes, the unyielded zones are thicker compared to the regions close to the line of $\pi/2$ between the x and y axes, which is mainly due to the stress concentration at the tips of the vane blades. Note that the Papanastasiou model is used in the present study for which the fluids flow at any shear rate. At low shear rate the viscosity is significantly higher, in that sense the fluid behaves similar to a shear thinning fluid. Near the vane blade tip the shear rate is highest therefore the corresponding apparent viscosity is small. It induces a shear thinning/localization layer in which the shear rates and stresses are highest. However, there is no shear localization in the region close to the line of $\pi/2$ between the two vane blades. As a consequence in the region away from the shear localization zone towards the outer wall along the x and y axes, the shear stress is lower compared to that in the regions between the two vane blades. If the stress is lower than the yield stress τ_0, the corresponding region is considered unyielded.

Figs. 15e and 16e show the normalized non-dimensional shear stress profiles along the line of $\pi/2$ between the x and y axes for Bingham fluids with different Bingham numbers under different applied angular velocities. The stress patterns for the two cases are similar: starting from the distance to the origin, $r = 0$, the shear stress increases from zero to reach a peak value when r is approximately equal to the vane blade length and then starts to decrease when r approaches the outer cylindrical boundary.

7. Conclusions

The objective of the present study was to determine the suitability of a vane rheometer for measuring rheological properties. A secondary objective was to validate the SPH approach for such flow a problem. A 2D SPH simulation was developed, and validated both theoretically and by comparison with experiment. Numerical tests, modeling the flow of Newtonian fluids were performed and the results were compared with experimental data. It was found that only a 6.5% difference existed between the experimental data and the simulation and this is considered acceptable bearing in mind that only a 2D simulation was used. The hypothesis that the vane acts as a cylinder with a Newtonian fluid is weak because the data obtained with the vane and the rotor differed by up to 29%, which is mainly due to the development of secondary flows between vane blades.

A parametric study for the flow of Bingham fluids with different Bingham numbers under various applied angular velocities of the outer cylinder wall was conducted. It was concluded that the Bingham number plays a crucial role in determining the torques transmitted to the outer wall of the vane rheometer. In general, larger values of Bingham number cause larger sizes of unyielded materials in the inner blade region and render the flow condition closer to that in a coaxial cylinder rheometer.

We believe that the Bingham number is not the only non-dimensional quantity that influences the flow field and hence the stress field. We therefore also conducted our simulations with relatively larger applied angular velocities. The shear rates considered in the present study are significantly higher than those published by other researchers [5,31]. Our numerical simulation shows that the angular velocity of the outer wall does affect the shear stress ratios between the vane and coaxial cylinder rheometers. For smaller Bingham numbers (<1), the shear stress ratio is larger at higher magnitudes of applied angular velocities; for larger Bingham numbers (>1.5), the shear stress ratio is lower at higher magnitude of applied angular velocities, while for Bingham numbers in the range of 1–1.5, the shear stress ratio differences between the vane and coaxial cylinder rheometers are quite small. As the magnitude of the applied angular velocity increases, the Reynolds number becomes larger, and hence the inertial force becomes more prominent relative to the viscous force. This possibly causes the small variation of stress ratios under different applied angular velocities.

This parametric study shows that the shear stress obtained for Bingham-like fluids in the vane and rotor geometries differed by up to 24% (Table 3) with the discrepancy decreasing with increasing Bingham numbers. This result shows that care should be taken in the interpretation of experimental data when use the vane rheometer to measure plastic viscosity. Specifically, if the Bingham number is larger, say greater than 2, the experimental data can be interpreted by assuming that there is a virtual cylinder within which the material moves with the blades. If the Bingham number is smaller, estimates of viscosity will have a tendency to be low, hence limiting the reliability of the vane rheometer to measure plastic viscosity. We also observe that the lower values of applied angular velocity favor the use of a vane rheometer to measure the rheological properties of Bingham fluids.

Finally, results from this study have served to further validate the SPH method for simulating flows of non-Newtonian fluids in complex geometries. Clearly the SPH method is a promising approach that can be used to simulate flow in other rheometer geometries, or include other features such as free surface or modeling rigid body flow in rheometers.

Acknowledgements

The authors wish to acknowledge financial support via NASA grant NNC06AA18A and John Winpigler for performing the experimental tests. We would also like to acknowledge support from the Virtual Cement and Concrete Testing Laboratory (VCCTL) consortium.

References

[1] Q.D. Nguyen, D.V. Boger, Yield stress measurement for concentrated suspensions, J. Rheol. 27 (1983) 321–349.
[2] H.A. Barnes, Q.D. Nguyen, Rotating vane rheometry—a review, J. Non-Newt. Fluid Mech. 98 (2001) 1–14.
[3] H.A. Barnes, J.O. Carnali, The vane-in-cup as a novel rheometer geometry for shear thinning and thixotropic materials, J. Rheol. 34 (1990) 841–866.
[4] J. Yan, A.E. James, The yield surface of viscoelastic and plastic fluids in a vane viscometer, J. Non-Newt. Fluid Mech. 70 (1997) 237–253.
[5] J.F. Keentok, M.J.F. Milthorpe, E. O'Donovan, On the shearing zone around rotating vanes in plastic liquids: theory and experiment, J. Non-Newt. Fluid Mech. 17 (1985) 23–35.
[6] D.V. Griffiths, P.A. Lane, Finite element analysis of the shear vane test, Comput. Struct. 37 (1990) 1105–1116.
[7] L.B. Lucy, A numerical approach to the testing of the fission hypothesis, Astron. J. 83 (1977) 1013–1024.
[8] R.A. Gingold, J.J. Monaghan, Smoothed particle hydrodynamics theory and application to non-spherical stars, Mon. Not. R. Astron. Soc. 181 (1977) 375–389.

[9] A. Colegrossi, M. Landrini, Numerical simulation of interfacial flows by smoothed particle hydrodynamics, J. Comput. Phys. 191 (2003) 448–475.
[10] X.Y. Hu, N.A. Adams, A multi-phase SPH method for macroscopic and mesoscopic flows, J. Comput. Phys. 213 (2006) 844–861.
[11] J.J. Monaghan, A. Kocharyan, SPH simulation of multi-phase flow, Comput. Phys. Commun. 87 (1995) 225–235.
[12] J.P. Morris, Simulating surface tension with smoothed particle hydrodynamics, Int. J. Numer. Methods Fluids 33 (2000) 333–353.
[13] L. Oger, S.B. Savage, Smoothed particle hydrodynamics for cohesive grains, Comput. Methods Appl. Mech. Eng. 180 (1999) 169–183.
[14] P.W. Cleary, M. Prakash, Discrete-element modelling and smoothed particle hydrodynamics: potential in the environmental sciences, Philos. Trans. R. Soc. Lond. A 362 (2004) 2003–2030.
[15] C. Antoci, M. Gallati, S. Sibilla, Numerical simulation of fluid–structure interaction by SPH, Comput. Struct. 85 (2007) 879–890.
[16] M. Ellero, M. Kroger, S. Hess, Viscoelastic flows studied by smoothed particle dynamics, J. Non-Newt. Fluid Mech. 105 (2002) 35–51.
[17] M. Ellero, R.I. Tanner, SPH simulation of transient viscoelastic flows at low Reynolds number, J. Non-Newt. Fluid Mech. 132 (2005) 61–72.
[18] J. Fang, R.G. Owens, L. Tacher, A. Parriaux, A numerical study of the SPH method for simulating transient viscoelastic free surface flows, J. Non-Newt. Fluid Mech. 139 (2006) 68–84.
[19] T.C. Papanastasiou, Flows of materials with yield, J. Rheol. 31 (1987) 385–404.
[20] A.N. Alexandrou, P. Le Menn, G. Georgiou, V. Entov, Flow instabilities of Herschel–Bulkley fluids, J. Non-Newt. Fluid Mech. 116 (2003) 19–32.
[21] G.R. Burgos, A.N. Alexandrou, V. Entov, On the determination of yield surfaces in Herschel–Bulkley fluids, J. Rheol. 43 (1999) 463–483.
[22] H. Zhu, D. De Kee, A numeric study for the cessation of Couette flow of non-Newtonian fluids with a yield stress, J. Non-Newt. Fluid Mech. 143 (2005) 64–70.
[23] J.P. Gray, J.J. Monaghan, R.P. Swift, SPH elastic dynamics, Comput. Mech. Appl. Mech. Eng. 190 (2001) 6641–6662.
[24] J.J. Monaghan, SPH without a tensile instability, J. Comput. Phys. 159 (2000) 290–311.
[25] W.H. Press, S.A. Teukolsky, B.P. Flannery, Numerical Recipe in C: The art of Scientific Computing, Cambridge University Press, Cambridge, 1992, p. 847.
[26] J.J. Monaghan, Smoothed particle hydrodynamics, Annu. Rev. Astron. Astrophys. 30 (1992) 543–574.
[27] J.P. Morris, P.J. Fox, Y. Zhu, Modeling low Reynolds number incompressible flows using SPH, J. Comput. Phys. 136 (1997) 214–226.
[28] J.J. Monaghan, Simulating free surface flows with SPH, J. Comput. Phys. 110 (1994) 399–406.
[29] S.J. Cummins, M. Rudman, An SPH projection method, J. Comput. Phys. 152 (1999) 584–607.
[30] F. Colin, R. Egli, F.Y. Lin, Computing a null divergence velocity field using smoothed particle hydrodynamics, J. Comput. Phys. 217 (2006) 680–692.
[31] M. Ellero, M. Serrano, P. Español, Incompressible smoothed particle hydrodynamics, J. Comput. Phys. 226 (2007) 1731–1752.
[32] M. Chatzimina, G.C. Georgiou, I. Argyropaidas, E. Mitsoulis, R.R. Huilgol, Cessation of Couette and Poiseuille flows of a Bingham plastic and finite stopping times, J. Non-Newton Fluid Mech. 129 (2005) 117–127.
[33] R.B. Bird, W.E. Stewart, E.N. Lightfoot, Transport Phenomena, John Wiley & Sons, Inc., 1960.
[34] M. Chatzimina, G. Georgiou, A. Alexandrou, Wall shear rates in circular Couette flow of a Herschel–Bulkley fluid, Appl. Rheol. 19 (3) (2009) 34288.
[35] C. Atkinson, J.D. Sherwood, The torque on a rotating n-bladed Vane in a Newtonian fluid or linear elastic, Proc. Math. Phys. Sci. 438 (1992) 183–196.
[36] S. Savamand, M. Heniche, V. Bechard, F. Bertand, P.J. Carreau, Analysis of the vane rheometer using 3-D finite element simulation, J. Rheol. 51 (2007) 161–177.
[37] C.F. Ferraris, L.E. Brower, Comparison of concrete rheometers: international tests at MB (Cleveland, OH, USA) in May, 2003, NISTIR 7154.
[38] M.P. Landry, I.A. Frigaard, D.M. Martinez, Stability and instability of Taylor–Couette flows of a Bingham fluid, J. Fluid Mech. 560 (2006) 321–353.